



**8th International Conference
on
Wind Turbine Noise
Lisbon – 12th to 14th June 2019**

**Numerical Investigation of the Porous Trailing Edge
Noise Reduction Mechanism using the Lattice-
Boltzmann Method**

**F. Manegar, University of Siegen, 57068 Siegen, Germany
E-Mail: farhan.manegar@uni-siegen.de**

**C. Teruna, Delft University of Technology, 2629HS Delft, The Netherlands
E-Mail: C.Teruna@tudelft.nl**

**F. Avallone, Delft University of Technology, 2629HS Delft, The Netherlands
E-Mail: F.Avallone@tudelft.nl**

**W. C. P. van der Velden, Dassault Systemes Deutschland GmbH, 70563
Stuttgart, Germany
E-Mail: wouter.vandervelden@3ds.com**

**D. Casalino, Delft University of Technology, 2629HS Delft, The Nether-
lands
E-Mail: D.Casalino@tudelft.nl**

**T. Carolus, University of Siegen, 57068 Siegen, Germany
E-Mail: thomas.carolus@uni-siegen.de**

**D. Ragni, Delft University of Technology, 2629HS Delft, The Netherlands
E-Mail: D.Ragni@tudelft.nl**

**A. Rubio Carpio, Delft University of Technology, 2629HS Delft, The Nether-
lands
E-Mail: A.RubioCarpio@tudelft.nl**

ABSTRACT

Permeable materials can be installed at the trailing edge of an airfoil to mitigate turbulent boundary layer trailing edge noise in the low frequency range. Goal of this study is to investigate the physical mechanisms behind trailing edge noise

reduction for a porous trailing edge. Numerical simulations are carried out and the results are validated against experimental data. The flow around a NACA 0018 airfoil at 0° angle of attack and at a chord-based Reynolds number equal to 2.8×10^5 is investigated. The transport phenomena within the porous region are reproduced with the Hazen-Dupuit-Darcy law, where the Darcian force coefficients are taken from experimental data. A comprehensive mesh study for both solid and porous trailing edges is conducted. The boundary layer integral parameters and the far-field sound pressure spectrum are in good agreement with the experiments. The noise reduction capability of the porous trailing edge is successfully predicted in the range of frequency of interest, however, simulations do not show the noise increase in the high frequency range, due to the absence of roughness in the computational setup adopted to model porosity. The spanwise correlation length of the pressure fluctuations close to the wall does not show any relevant difference between the solid and the porous trailing edge thus suggesting that the large scale structures are not affected by the porous insert.

1. INTRODUCTION

Airfoil self-noise is the major noise source in wind turbine applications [1]. In particular, turbulent boundary layer trailing edge (TBL-TE) noise, generated by the scattering of turbulent flow at the trailing edge [2] is the dominant noise mechanism [3]. The most common technique employed by wind turbine manufacturers is the installation of saw-tooth shaped serrations at the trailing edge to reduce TBL-TE noise. Other noise-reduction techniques are being developed to achieve noise reduction, such as, active boundary-layer suction system [4], porous trailing edges [5] and blade shape optimization [6].

Dedicated porous materials, typically applied to a certain percentage of the chord length, are made by a uniform and permeable structure with interconnected pores. The permeability typically reduces the impedance jump at the edge, with a consequent reduction of the radiated noise. Noise reduction capabilities of porous materials have been successfully demonstrated in several aerodynamic applications [7]. Porous materials are conventionally characterized with porosity and flow resistivity. Geyer *et al* [7] carried out an extensive set of measurements, using different materials and different streamwise extensions, but they did not find any exhaustive correlation between porous material characteristics and their noise levels. They found though that with a longer extension of the porous material, a larger measured noise reduction is achieved, together with a degradation of the aerodynamic properties (i.e., lift and drag).

More recently, Rubio-Carpio *et al* [8] investigated, using microphone array and time-resolved Particle Image Velocimetry (PIV) measurements, a NACA 0018 profile with a porous trailing edge made of metal foams. Several foams with different properties (i.e., porosity and flow resistivity) were investigated. Noise reduction was measured at lower to middle frequency (from 500 to 1600 Hz), while noise increase, attributed to the surface roughness, was found at higher frequencies. The effects of the flow connection through metal-foam on far-field acoustics was tested by adding a non-permeable layer [9]. For this configuration, no noise reduction was measured at lower to mid frequency, but noise increase in the higher frequencies was still present.

In this study, the experimental study of Rubio Carprio *et al* [8] is investigated numerically using the commercial software 3DS-Simulia™ PowerFLOW.

Since it is computationally expensive to simulate the entire geometry at the porous trailing edge, a porous media formulation is used.

2. COMPUTATIONAL METHOD

2.1 Flow solver

The lattice-Boltzmann (LB) commercial solver 3DS-Simulia™ PowerFLOW version 5.4b has been used because it has been proved to be reliable for trailing edge noise prediction [10, 11]. The LBM solves the Boltzmann equation on a Cartesian mesh, named as lattice. The discretization used for this particular application consists of 19 discrete velocities in three dimensions (D3Q19), involving a third-order truncation of the Chapman-Enskog expansion. The equations are solved with an explicit time integration approach and the stability of the solution is obtained by setting the Courant-Friedrichs-Lewy stability number to unity. To obtain the particle distribution, a collision term, based on a unique Galilean invariant [12], and an equilibrium distribution of Maxwell-Boltzmann [13] are adopted.

A Very Large Eddy Simulation (VLES) model is implemented to consider the effect of the sub-grid unresolved scales of turbulence. Following [14], a two-equations *k-epsilon* renormalization group is used to compute a turbulent relaxation time that is added to the viscous relaxation time. In order to reduce the computational cost, a pressure-gradient-extended wall-model is used to approximate the no-slip boundary condition on solid walls [15, 16]. The model is based on the extension of the generalized law-of-the-wall model [17] to consider the effect of pressure gradient.

A Darcy's porous media formulation is used to compute the flow within the foam. The parameters that characterize the macroscopic properties of transport phenomena within a porous material are: porosity, permeability and form coefficient. The porosity of the material is defined as:

$$\phi = 1 - \frac{\rho_p}{\rho_s} \quad (1)$$

where ρ_p and ρ_s are the density of the porous material and of the solid, respectively. In porous media, the Hazen-Dupuit-Darcy equation describes the pressure loss Δp when certain mass flow permeates through a porous material sample of thickness h :

$$\frac{\Delta p}{h} = \frac{\mu_\infty}{K} v_d + \rho_\infty C v_d^2 \quad (2)$$

where μ_∞ and ρ_∞ is the fluid's freestream dynamic viscosity and density respectively. K and C are the permeability and the form coefficient of the porous material. The coefficients of the Darcian velocity v_d (eq. 2) are defined as viscous ($R_V = \mu_\infty / \rho_\infty K$) and inertial ($R_I = C$) resistance. The pressure gradient ∇p through a porous material is proportional to the local flow velocity u , as follows:

$$\nabla p = -R \cdot u \quad (3)$$

where R is the sum of viscous and inertial resistivity components (R_V and R_I respectively). This law is then applied in the LBM solver and readers are referred to [18] and [19] for a more detailed description.

The viscous and inertial resistances are taken from the experimental study conducted by Rubio Carpio *et al* [8].

2.2 Noise computation

The compressible and time-dependent nature of the transient CFD solution together with the low dissipation and dispersion properties of the LB scheme allow extracting the sound pressure field directly in the near-field up to a cut-off frequency corresponding to approximately 15 voxels per acoustic wavelength [20]. In the far field, noise is computed by using the Ffowcs Williams and Hawkings (FW-H) equation [21]. The formulation 1A, developed by Farassat [22] and extended to a convective wave equation is used in this study [23, 24]. The formulation is implemented in the time domain using a source-time dominant algorithm [25]. To compare computational results and simulations the scaling adopted in [11] is used:

$$L_{S_{pp},scaled} = L_{S_{pp}} + 10 \log_{10} \left[\left(\frac{R}{R_c} \right)^2 / \left(\left(\frac{b}{b_c} \right) \left(\frac{M}{M_c} \right)^5 \right) \right]. \quad (4)$$

where $R_c = 1$ m, $M_c = 1$ and $b_c = 1$ m, that are the reference listener location, Mach number and span of the airfoil.

3. NUMERICAL CASE SETUP

A two-dimensional NACA 0018 airfoil has been investigated. It has a chord length $c = 200$ mm and a span of $b = 40\%c$ (80 mm). Transition is forced at $20\%c$ with a zig-zag trip with thickness of 0.6 mm, spanwise periodicity of 2.9 mm and length of 3.6 mm. The transition technique adopted here, though different from the actual experimental realization, has been found to be the one that best represents both the BL thickness and energy cascade.

The freestream velocity is $U_\infty = 20$ m/s, corresponding to a chord-based Reynolds number of 2.8×10^5 . The effective angle of attack is $\alpha_{eff} = 0^\circ$, making it a zero-lift setup.

Fig. 1 shows a schematic of the simulation domain (not in scale). The reference coordinate system has its origin at the trailing edge of the airfoil ($X/c = 0$), where X and Y axes are aligned with the chord direction and its normal direction respectively.

The numerical grid consists of 10 zones of variable resolution (VR). Each VR zone consists of cubical volume cells called voxels. The size of voxels increases by a factor of two in adjacent VR zones. The VR zone containing the finest voxel is around the airfoil. The simulation domain is $100c$ long in the X and Y -axis. The airfoil is placed at the center of the simulation domain. The details regarding the number of voxels, time step corresponding to finest voxel resolution and computation time is provided in the next section, where different mesh resolutions are investigated.

Boundary conditions are provided in terms of velocity and pressure at all four boundaries (free-field boundary conditions) of the simulation domain in the X - Y plane, with periodic boundary conditions applied along the Z -axis. As seen in Fig. 1, for the porous configuration, a 1 mm thick outer layer of acoustics porous medium (APM) surrounding the porous medium (PM) is used at the trailing edge. Both medium applied in PowerFLOW describe the porous material as an equivalent fluid region with resistance governed by the Darcian forces. In addition to this, the APM also considers the acoustic absorption property of the material and governs the mass flow between the regular fluid region and the APM

region through a porosity value. The simulated Mach number ($M = 0.0588$) is chosen to be the same as in the experiment. An anechoic outer layer is specified starting from a radius of $36c$ from the airfoil center to damp outward traveling acoustic waves and to prevent reflection by the domain boundaries.

All the mean and unsteady quantities shown in the mesh resolution study and results sections are evaluated with a sampling rate $f_s = 20$ kHz and are recorded for 10 flow passes (c/U_∞) (corresponding to a physical time of 0.1 s). They are evaluated at the red and blue dotted lines shown in Fig.2 for boundary layer and wake flow respectively. The far-field noise calculated from airfoil surface and FW-H permeable surface are evaluated with a sampling rate $f_{s,a} = 248$ kHz and are recorded for 10 flow passes as well.

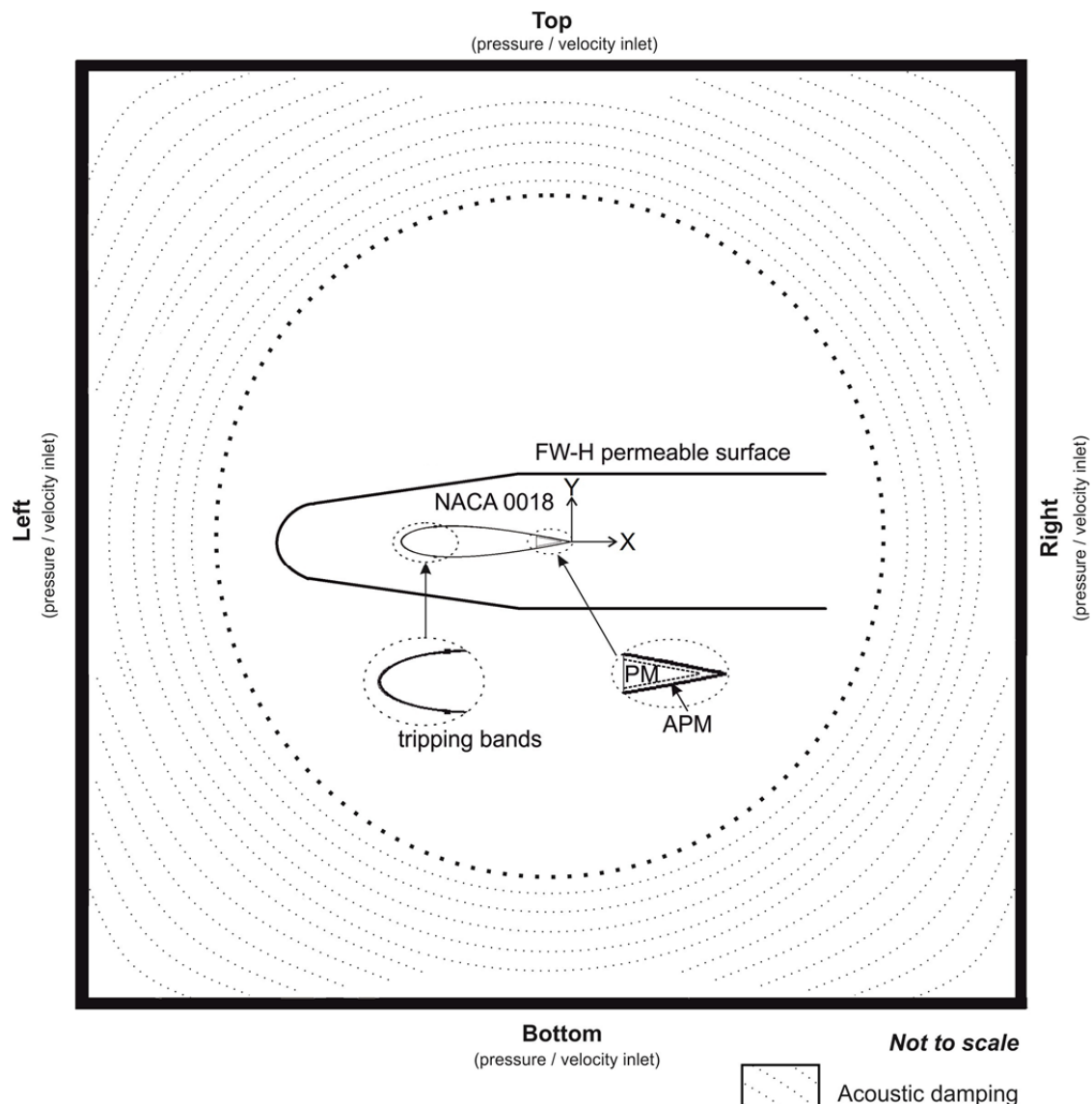


Figure 1. Schematic of airfoil segment and simulation domain in LBM (not to scale).

Mesh study

A mesh independence study is conducted aiming at evaluating the sensitivity to the voxel size and their distribution. The investigated configurations are named based on the surface y^+ value at the trailing edge. Table 1 reports the

finest voxel size for each configuration, the corresponding time step, total number of voxels, total number of fine equivalent voxels (average number of voxels updated each time step) and the resulting computational time. The mesh configuration ' $y^+ = 3$ (only in the vicinity of the trip)' has the same distribution of VR zones as ' $y^+ = 3$ ', but with refinement applied only in the vicinity of the trip.

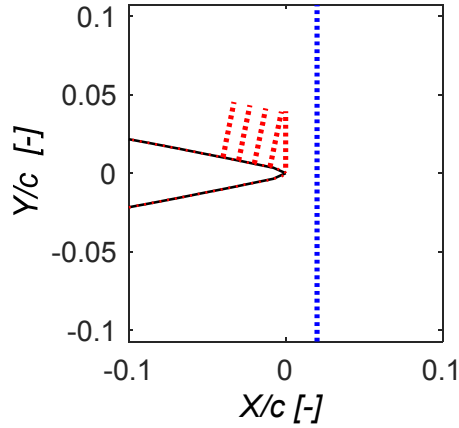


Figure 2. Locations at which velocity field data are sampled – red dotted lines: for the boundary layer, blue dotted lines: for the wake.

The configurations ' $y^+ = 3$ ' and ' $y^+ = 2.25$ ' differs only for the finest voxel size while keeping the same VR distribution. For the latter configuration, in order to reduce the computational costs, the span is decreased to $30\%c$, unlike the other two configurations where it is $40\%c$. Fig. 3 shows the mesh around trip region for the three configurations.

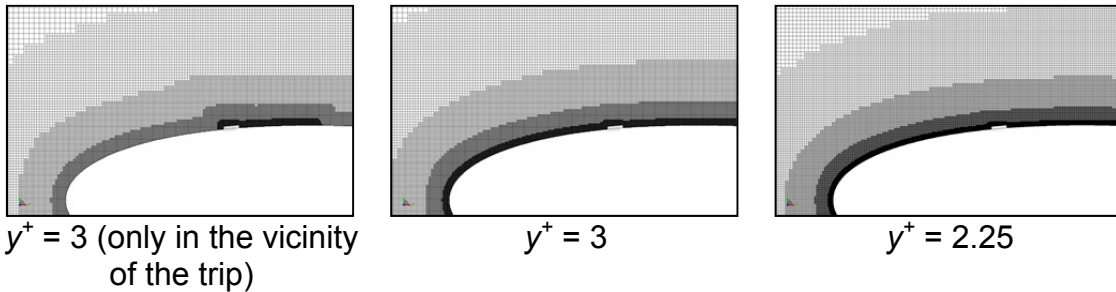


Figure 3. Mesh generated around trip on suction side for the different mesh configurations.

Table 1. Mesh study details for solid trailing edge.

Parameters	$y^+ = 3$ (only in the vicinity of the trip)	$y^+ = 3$	$y^+ = 2.25$ (span = $30\%c$)
Finest voxel size (m)	7.81e-05	7.81e-05	5.86e-05
No. of voxels (million)	90	243	308
No. of fine equivalent voxels (million)	40	170	217
Smallest time step (s)	1.299e-07	1.299e-07	9.742e-08
Computational time (CPU hours) per flow pass on an Intel Xeon Haswell EP E5-2630v3 platform	1137	2880	4800

First the unsteady flow quantities are compared with experimental data for the two coarser mesh configurations, namely ‘ $y^+ = 3$ (only in the vicinity of the trip)’ and ‘ $y^+ = 3$ ’ to assess the influence of the grid on the flow development. This comparison is only performed for the solid trailing edge. Fig. 4 (left) shows the power spectral density of wall-parallel velocity fluctuations $|\Phi_{uu}|$ measured above the trailing edge at $Y/c = 0.017$ against the chord-based Strouhal number $St = fc/U_\infty$. Fig. 4 (right) shows the profile of root mean squared (R.M.S) values of the wall-parallel velocity (u) above the trailing edge, normalized with U_∞ .

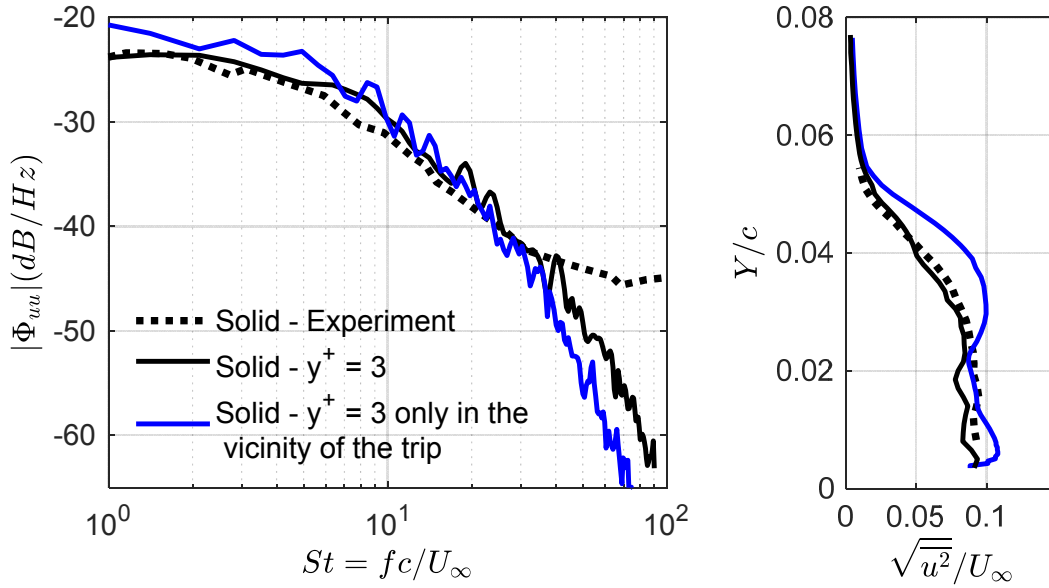


Figure 4. Comparison of ‘ $y^+ = 3$ ’ and ‘ $y^+ = 3$ (only in the vicinity of the trip)’ with experiment (only for solid trailing edge). Left: Power spectral density of wall-parallel velocity fluctuations $|\Phi_{uu}|$ ($X/c = 0$, $Y/c = 0.017$). Right: Profile of R.M.S of wall-parallel velocity fluctuations above trailing edge.

From Fig. 4 (left) it is evident that the mesh configuration ‘ $y^+ = 3$ (only in the vicinity of the trip)’ show more energy at lower frequencies (below $St = 10$) compared to experiment. The R.M.S of the streamwise velocity shows a broad peak between $Y/c = 0.03$ to 0.05 that is associated to the energy content discussed before. Refining the mesh uniformly around the airfoil solves the problem and a better agreement is found with the experiments. The peak for the ‘ $y^+ = 3$ (only in the vicinity of the trip)’ is associated to turbulent structures generated by the zig-zag trip not sufficiently dissipated.

The convergence between mesh configuration ‘ $y^+ = 3$ ’ and ‘ $y^+ = 2.25$ ’ is further studied by comparing the unsteady wall-parallel and wall-normal velocity components as shown in Fig.5 and Fig.6, respectively. Spectra of the wall-parallel $|\Phi_{uu}|$ and wall-normal velocity fluctuations $|\Phi_{vv}|$ shown on the left side of the figures show grid independence. The R.M.S values shown on the right side of the figures show reasonable convergence in the case of solid trailing edge but some deviation in the porous trailing edge. It has to be mentioned that the simulation run for the ‘ $y^+ = 2.25$ ’ mesh configuration only ran for a limited time

instant due to excessive costs. From these plots, the mesh configuration ' $y^+ = 3$ ' is chosen for the remainder of this study.

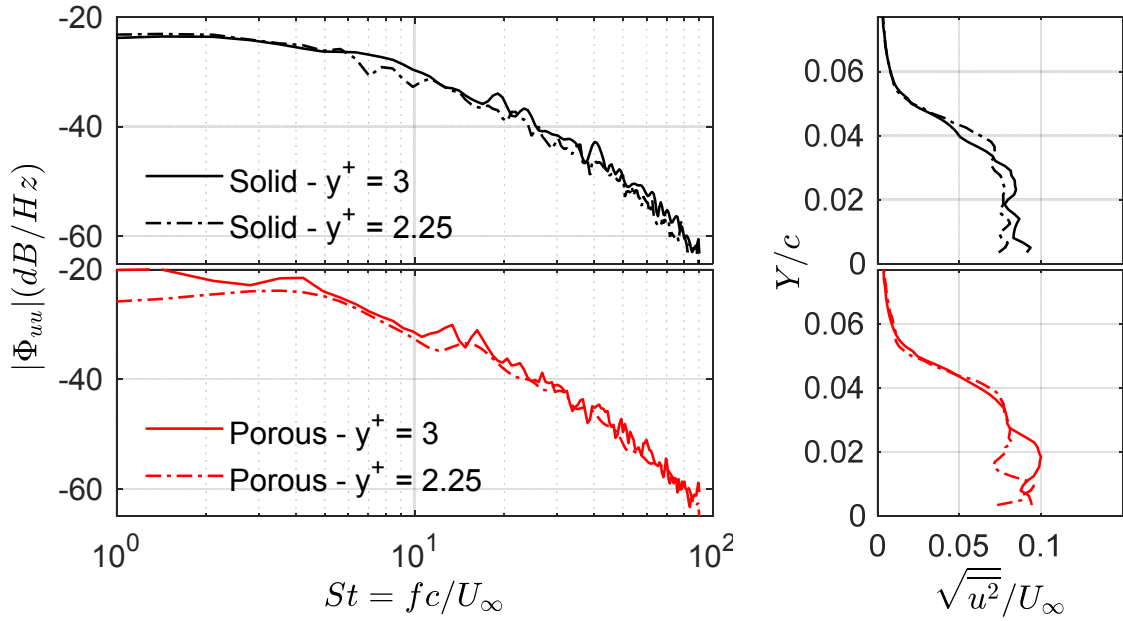


Figure 5. Mesh convergence study; left: Power spectral density of wall-parallel velocity fluctuations $|\Phi_{uu}|$ ($X/c = 0$, $Y/c = 0.017$); right: Profile of R.M.S of wall-parallel velocity fluctuations above trailing edge.

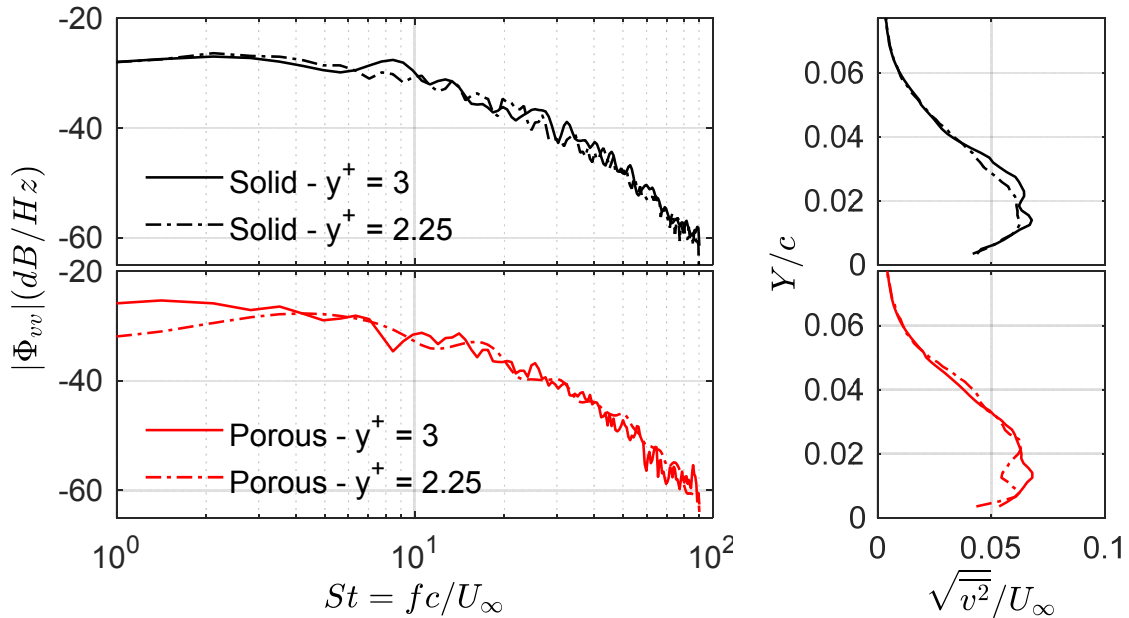


Figure 6. Mesh convergence study; left: Power spectral density of wall-normal velocity fluctuations $|\Phi_{vv}|$ ($X/c = 0$, $Y/c = 0.017$); right: Profile of R.M.S of wall-normal velocity fluctuations above trailing edge.

4. RESULTS

4.1 Comparison with the experimental results

Boundary layer statistics

Experiments have shown that a porous trailing edge leads to the development of a thicker boundary layer compared to a solid trailing edge [8, 26]. The reason for this phenomenon is attributed to roughness effects explained by Rubio Carpio *et al* [8] and to material resistivity explained by Geyer *et al* [26]. Simulation results show the same behavior as seen in the experiments. The boundary layer thickness (δ_{99}), displacement thickness (δ^*) and momentum thickness (θ^*) from simulations are validated against experimental results in Fig. 7. These integral quantities are then calculated as done in [8] (Fig. 2). δ_{99} is defined as the point where the wall-parallel velocity is 99% of the edge velocity (U_e). The agreement between the simulation and experiment is very good for the solid trailing edge case, while a slight disagreement is found for the porous trailing edge case.

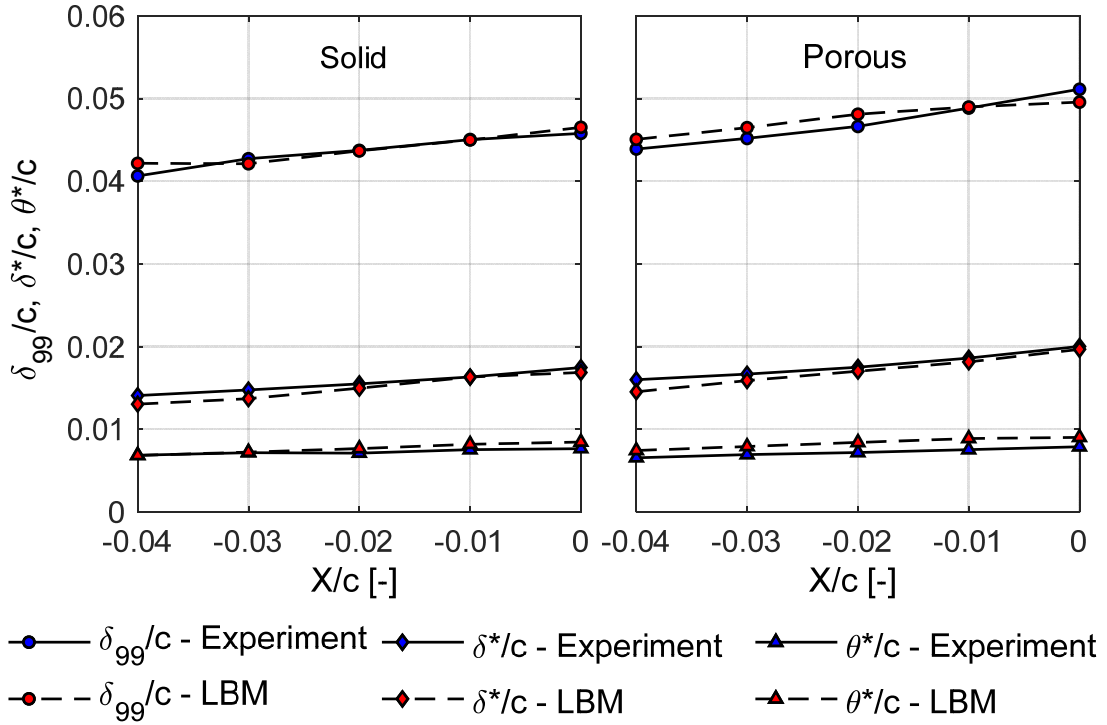


Figure 7. Boundary layer statistics showing boundary layer thickness (δ_{99}), boundary layer displacement thickness (δ^*) and momentum thickness (θ^*) on the suction side.

Even though in [8], the reason for increase in boundary layer of porous trailing edge is attributed to the deficit in the mean wall parallel velocity profile caused by roughness of the material, the simulation results here shows tendencies in favor of the explanations provided in [26]. As there is no roughness quantity modeled in the simulation, the increase in boundary layer for porous material could indeed be due to the resistivity properties of porous material.

Mean and turbulence quantities

In this section the mean and turbulence statistics obtained from simulations are compared against experiments. Simulation data are extracted and

processed at the trailing edge ($X/c = 0$), i.e. along the red dotted lines shown in Fig. 2. Fig. 8 shows the validation for a solid and porous trailing edge.

Profiles of the time-average wall-parallel velocity component u normalized with U_∞ are shown in Fig. 8 (left). A trend similar to the experiment is observed in the simulation. The porous trailing edge shows a slightly lower velocity compared to solid trailing edge for a given non-dimensional wall normal location. This difference was attributed to a higher surface drag.

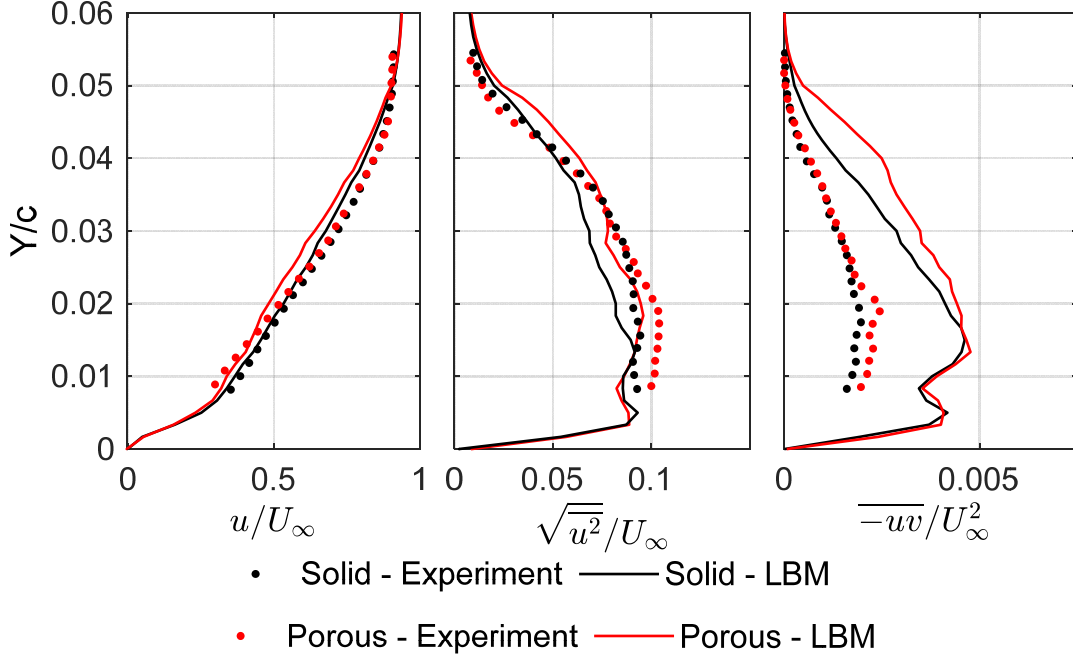


Figure 8. Mean and turbulence quantities at trailing edge ($X/c = 0$) on suction side.

The R.M.S profiles of wall-parallel velocity ($\sqrt{u^2}$) normalized with U_∞ are shown in the middle plot of Fig. 8. For both solid and porous trailing edge, a reasonable good agreement is found with simulations capturing larger turbulent fluctuations with respect to the solid trailing edge.

The Reynolds stresses $\overline{-uv}$ normalized with U_∞ obtained from the simulations are larger than the experimental one. This disagreement, due to an over estimation of the fluctuations of the wall-normal velocity component (v), might be attributed to the different tripping used in the experiments. However, an experimental malfunction should also not be neglected, as this component is often difficult to be extracted and averaged from planar PIV data. Therefore, further research on this aspect is necessary. Nevertheless, the trends captured from simulations are similar to the experimental ones; the porous trailing edge generates larger fluctuations near to the wall compared to the solid trailing edge. This phenomenon is speculated in [8] to be due to the unsteady cross-flow through the porous material.

Computational data extracted in the wake ($X/c = 0.02$, at the blue dotted lines shown in Fig.2) are compared with the experiments in Fig. 9. As in the experiment, the porous trailing edge has a minor effect on the near wake flow showing only a small increase of the velocity fluctuations.

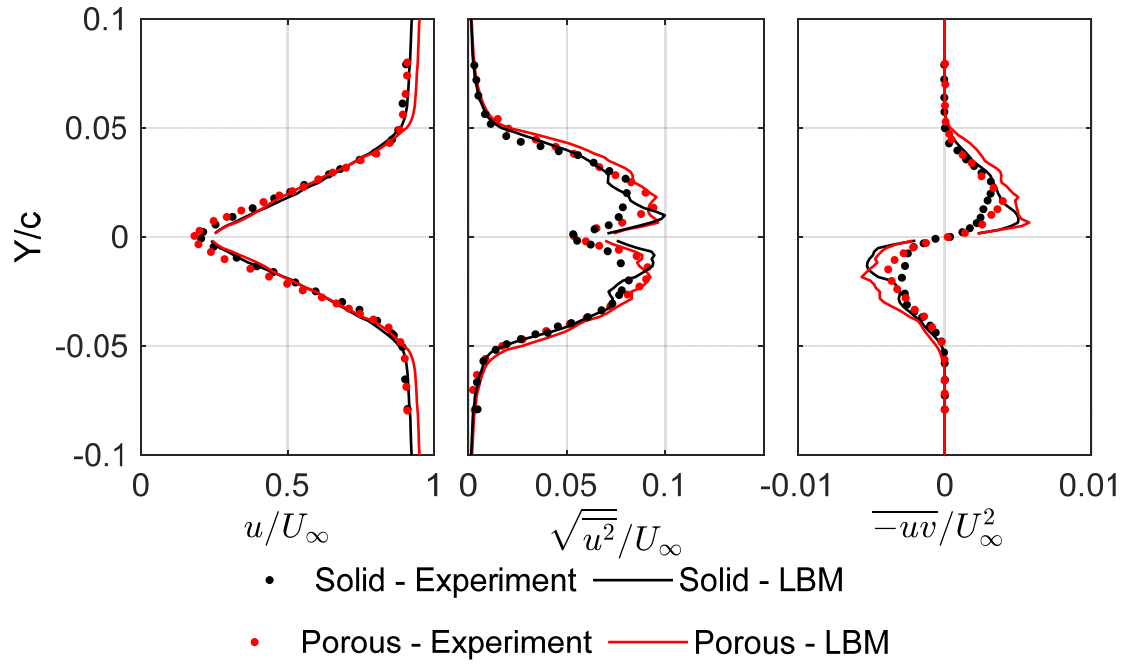


Figure 9. Mean and turbulence quantities in the near wake ($X/c = 0.02$).

Velocity fluctuation spectrum

The visualization of the instantaneous vorticity magnitude at the mid-span plane is shown for both configurations in Fig. 10. A qualitative comparison of the two figures show that the porous trailing edge weakly affect the large scale flow structures, in agreement with the previous results where only a minor difference in the amplitude of the turbulent fluctuations was found.

To verify if the porous materials affect the small scale structures, spectra of the wall-parallel velocity fluctuations at the trailing edge ($X/c = 0$, $Y/\delta_{99} = 0.3$) are shown in Fig. 11 for the u component and in Fig. 12 for the v component. As for the previous case a good agreement is found with the experiments; the porous trailing edge shows higher energy associated at low St number (less than 10), in agreement with the flow visualization. The only difference with the experiments, still related to the roughness effect, is the St number at which the two curves cross each other. In the simulation no cross-over St number is found and the two spectra are similar for $St > 10$. In the experiments the curves cross each other at $St = 15$.

Fig. 12 shows the spectral content of wall-normal velocity (v) fluctuations at $X/c = 0$ and $Y/\delta_{99} = 0.3$. As expected from the Reynolds stress profiles large energy content is present in the simulations with respect to the experiments. However, also in this case the energy distribution between the two configurations is similar.

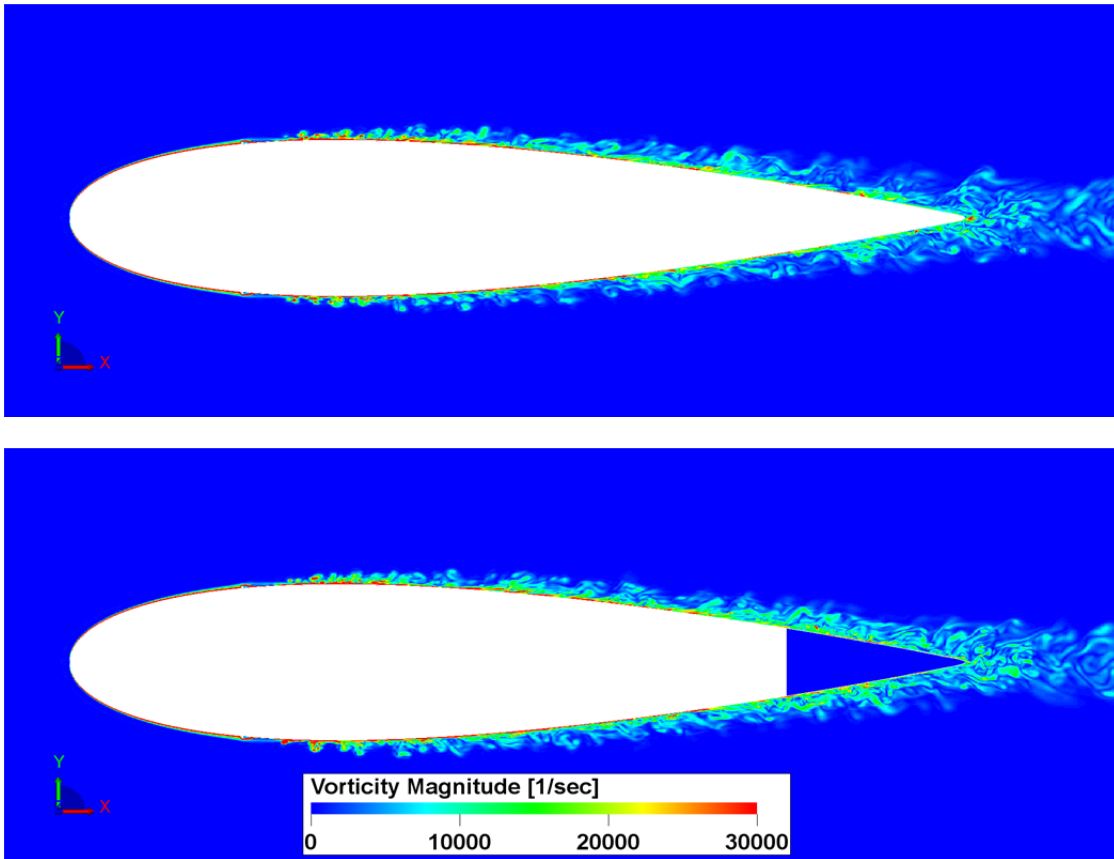


Figure. 10 Instantaneous vorticity magnitude fields at mid-span. Top – Solid trailing edge, bottom – porous trailing edge.

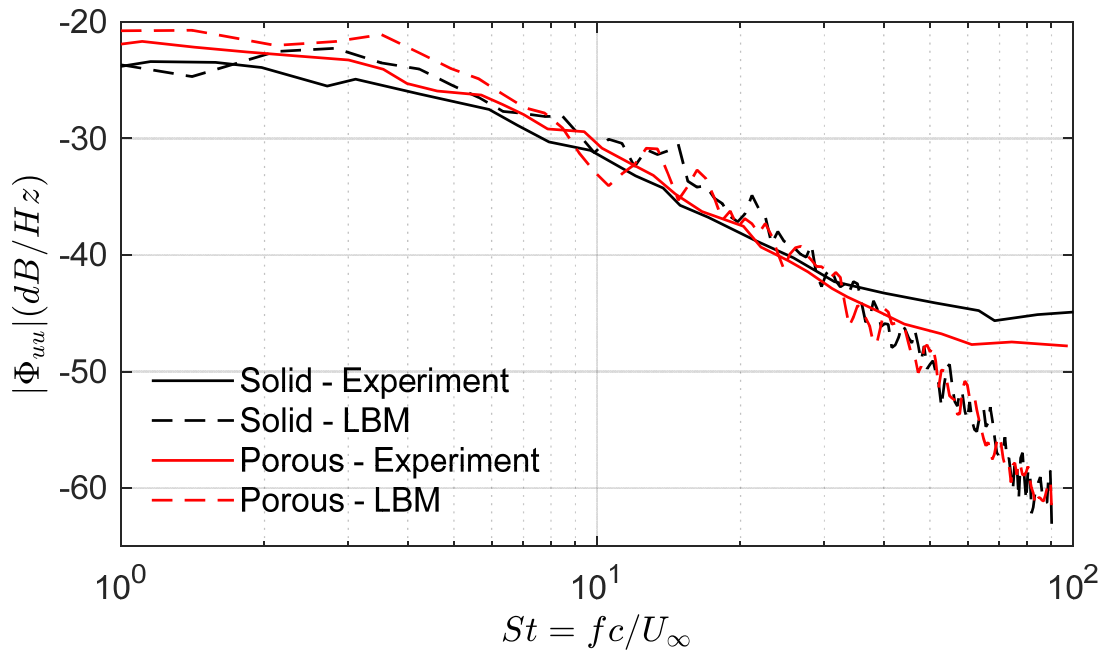


Figure. 11 Power spectral density of the wall-parallel velocity fluctuations at $X/c = 0$, $Y/\delta_{99} = 0.3$.

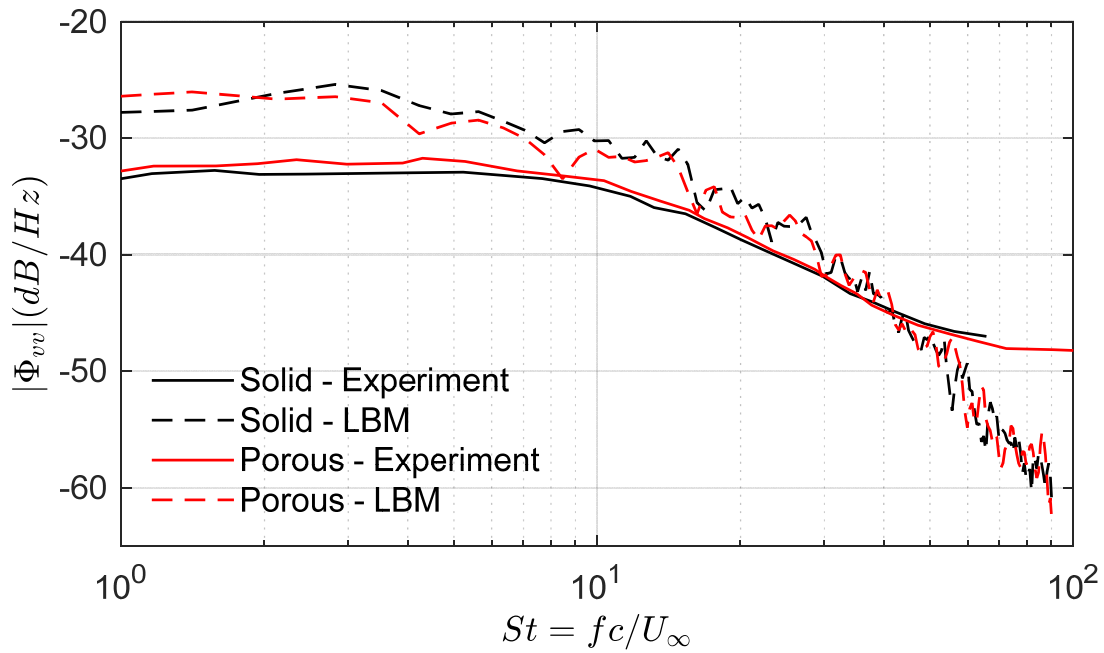


Figure. 12 Power spectral density of the wall-normal velocity fluctuations at $X/c = 0$, $Y/\delta_{99} = 0.3$.

Acoustics

Far-field acoustic results are plotted in Fig. 13 where the far-field spectra are scaled according to eq. 4.

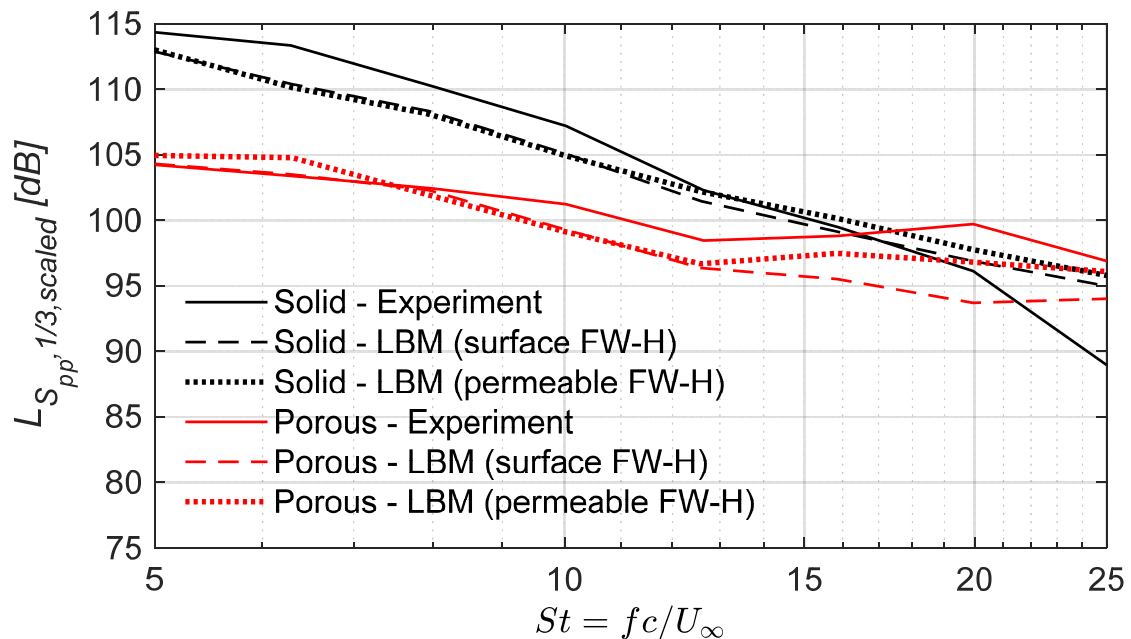


Figure. 13 Far-field sound pressure level between airfoils with solid and porous trailing edge.

The simulation predicts well the noise reduction capability of a porous trailing edge up to $St = 16$. The prediction for solid trailing edge is 2 dB less than the experiment, but on the whole the tendency is correct. Above $St = 16$ noise increase for the porous trailing edge is not found, whereas this is clearly

present in the experiment. As stated in [8], this experimental noise increase is attributed to the roughness of porous material. In the simulation, only the properties of porous material are modeled while the surface roughness is not, which is most likely the case why the noise increase is not observed in the simulation results.

Directivity plots from simulations are shown in Fig. 14. They are obtained using 72 microphones equally spaced in a circle of radius equal to $7.4c$ at the airfoil mid-span. The far-field noise is further integrated over the non-dimensional frequency band reported in each plot. No experimental comparison is available. In the frequency range $4 < St < 16$ (where the porous trailing edge shows noise reduction) both configuration show a compact dipole. The porous trailing edge shows almost the same noise reduction tendency for all angles. However, in the frequency range $16 < St < 32$, there is almost no difference between the two configurations. The results show that the presence of a porous medium does not alter the directivity pattern, thus suggesting that the mechanisms behind the noise scattering are similar for the two configurations.

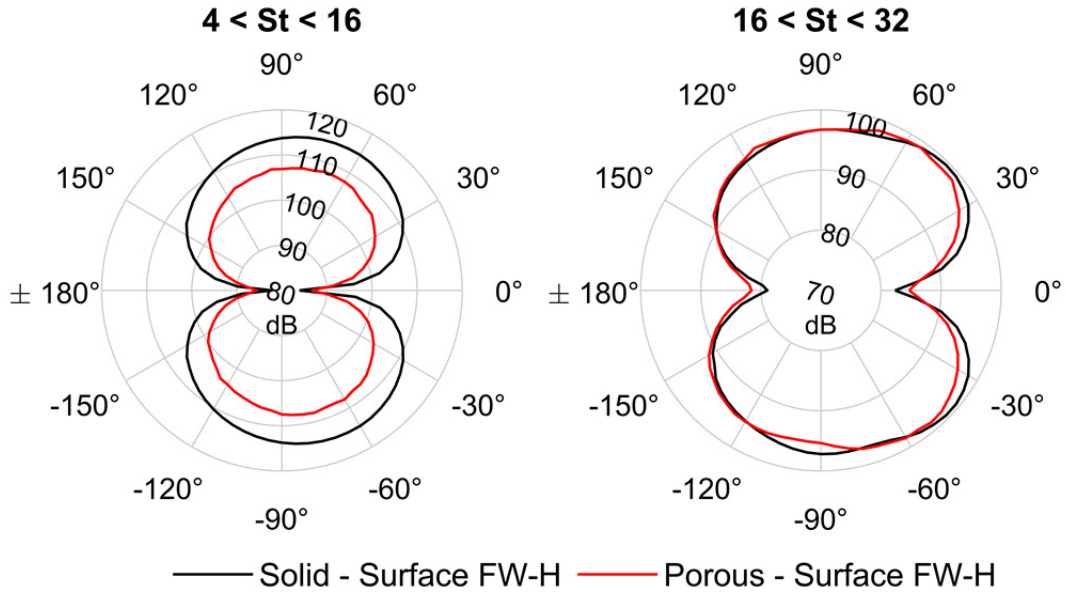


Figure. 14 Directivity plots of $L_{S_{pp},scaled}$ for the solid and porous trailing edge at two different non-dimensional frequency ranges: (left) $4 < St < 16$, (right) $16 < St < 32$.

4.2 Spanwise correlation length

Showkat Ali *et al* [27] reported that an internal hydrodynamic field within the porous material is present due to the penetration of the boundary layer flow within the porous material. This might alter the integral length scale of the turbulent structures. The spanwise correlation length (l_z) of the pressure fluctuations at 0.1 mm away from the wall, is calculated at various streamwise positions and plotted in Fig. 15. l_z is defined as:

$$l_z(x, f) = \int_{-\infty}^{\infty} \sqrt{\gamma^2(x, \Delta z, f)} dz \quad (5)$$

where γ^2 is the magnitude-squared coherence evaluated along the spanwise direction Z . Δz is the spanwise distance between the reference point and any other point along the span. γ^2 is computed with a periodogram approach using a Hanning window and 50 % overlap, and the resulting frequency resolution is 300 Hz.

An increase of l_z is found for configurations moving toward the trailing edge. More interestingly, only minor variations are found between the two configurations, thus suggesting that the flow is almost not affected by the presence of the porous medium.

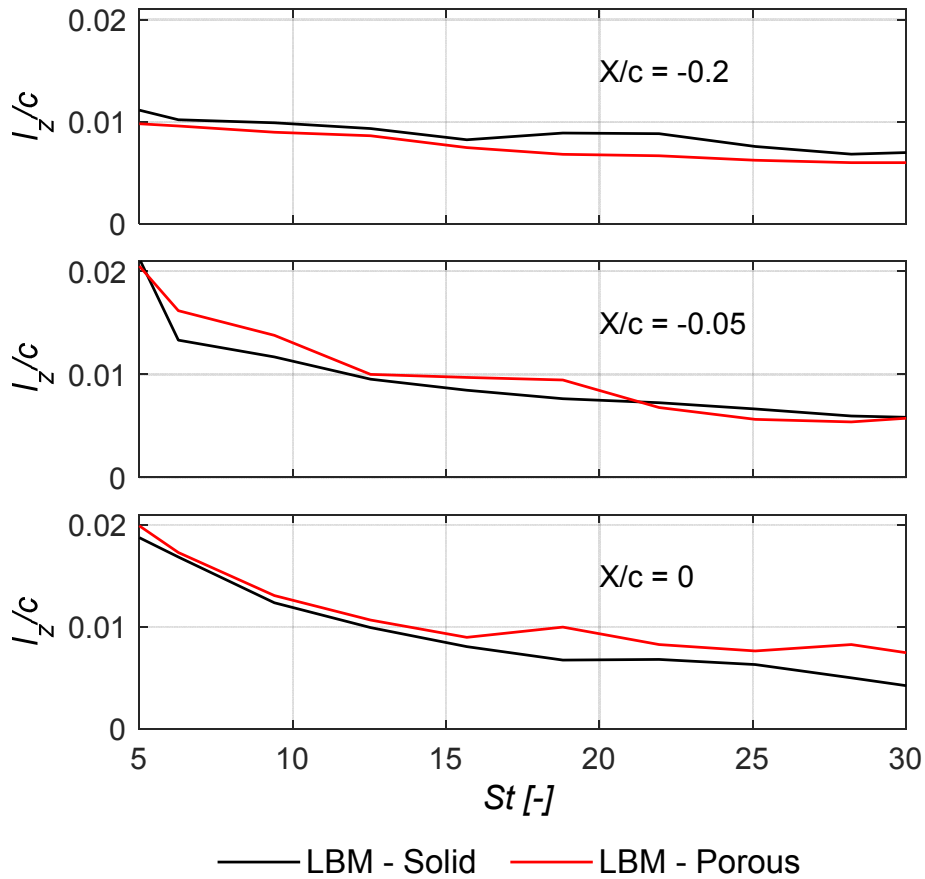


Figure. 15 Spanwise correlation length computed at 0.1 mm away in the wall-normal direction using pressure data.

In conventional trailing edge noise theory (Amiet [28]), l_z is one of the two most relevant parameters directly proportional to the noise radiation, where a larger l_z results in higher far-field noise. Since l_z is almost equal between the two configurations and the amplitude of the surface pressure fluctuations is larger for the porous trailing edge [8], confirmed here by the larger wall-normal velocity fluctuations, suggest that the Amiet's theory cannot be applied in this context. For this reason, the mitigation of the impedance mismatch between the two sides of the airfoil needs additional investigations. High fidelity simulations are therefore required and essential for this investigation.

5. CONCLUSIONS

Aeroacoustic Lattice-Boltzmann simulations of the flow around a NACA 0018 airfoil with solid and porous trailing edge are conducted successfully and

validated against available experimental data. The transport phenomena within the porous region are reproduced with the Hazen-Dupuit-Darcy law, where the Darcian force coefficients are taken from existing experimental data. A comprehensive mesh study is conducted and a mesh resolution with resulting $y^+ = 3$ at the trailing edge is chosen and further analyzed throughout the study. A very good agreement is achieved between simulation and experiment for the boundary layer integral parameters and turbulence statistics, except for the wall-normal velocity fluctuations. The noise reduction capability of the porous trailing edge is successfully predicted in the simulation, but the phenomenon of noise increase observed at experiment is not captured by simulation - most likely owing to the roughness of porous material that is not modeled. Finally, the spanwise correlation length (l_z) of the pressure fluctuations in the wall-normal direction, is analyzed at various streamwise positions. It is observed that the flow structures are not strongly influenced by the porous medium.

6. ACKNOWLEDGEMENTS

Financial support for this work was partly provided by the Federal Ministry for Economic Affairs and Energy of Germany (BMWi) within the project RENEW (FKZ 0325838B).

We acknowledge gratefully Dassault Systemes Deutschland GmbH for providing the licenses and technical assistance to carry out the LBM simulations.

The first author thanks the TU Delft group for hosting him as visiting researcher in 2018/19 for eight weeks.

7. REFERENCES

1. T. F. Brooks, D. S. Pope and M. A. Marcolini, *"Airfoil Self-Noise and Prediction"*, NASA Reference Publication, NASA-RP-1218 (1989)
2. M. S. Howe, *"A review of the theory of trailing edge noise"*, Journal of Sound and Vibration, Volume 61, No. 3, pp. 437-465 (1978)
3. S. Oerlemans, P. Sijtsma and B. Méndez López, *"Location and quantification of noise sources on a wind turbine"*, Journal of Sound and Vibration, Volume 299, Issues 4–5 (2007)
4. B. Arnold, Th. Lutz and E. Krämer, *"Design of a boundary-layer suction system for turbulent trailing-edge noise reduction of wind turbines"*, Renewable Energy, Volume 123, Pages 249-262 (2018)
5. T. Geyer and E. Sarradj, *"Trailing Edge Noise of Partially Porous Airfoils"*, 20th AIAA/CEAS Aeroacoustics Conference Atlanta, GA (2014)
6. S. Oerlemans, M. Fisher, T. Maeder and K. Kögler, *"Reduction of Wind Turbine Noise Using Optimized Airfoils And Trailing-Edge Serrations"*, 14th AIAA/CEAS Aeroacoustics Conference (29th AIAA Aeroacoustics Conference), Vancouver, British Columbia, Canada (2008)
7. T. Geyer, E. Sarradj and C. Fritzsche, *"Measurement of the noise generation at the trailing edge of porous airfoils"*, Experiments in Fluids, Vol. 48, No. 2, pp 291-308 (2010)
8. A. Rubio Carpio, R. Merino Martinez, F. Avallone, D. Ragni, M. Snellen and S. van der Zwaag, *"Broadband trailing-edge noise reduction using permeable metal foams"*, INTER-NOISE and NOISE-CON Congress and Conference Pro-

- ceedings, Vol. 255, Institute of Noise Control Engineering, pp. 2755-2765 (2017)
9. A. Rubio Carpio, F. Avallone and D. Ragni, “*On the role of the flow permeability of metal foams on trailing edge noise reduction*”, AIAA/CEAS Aeroacoustics Conference (2018)
 10. F. Avallone, W. van der Velden and D. Ragni, “*Benefits of curved serrations on broadband trailing-edge noise reduction*”, Journal of Sound and Vibration, Vol. 400, pp. 167-177 (2017)
 11. F. Avallone, W. van der Velden, D. Ragni and D. Casalino, “*Noise reduction mechanisms of sawtooth and combed-sawtooth trailing-edge serrations*”, Journal of Fluid Mechanics, Vol. 848, pp. 560–591 (2018)
 12. H. Chen, R. Zhang and P. Gopalakrishnan, “*Lattice Boltzmann Collision Operators Enforcing Isotropy and Galilean Invariance*”, (aug 2015)
 13. H. Chen, S. Chen and W. Matthaeus, “*Recovery of the Navier-Stokes equations using a lattice-gas Boltzmann method*”, Physical Review A, Vol. 45, No. 8, pp. R5339–R5342. doi:10.1103/PhysRevA.45.R5339 (1992)
 14. V. Yakhot and S. Orszag, “*Renormalization group analysis of turbulence. I. basic theory*”, Journal of Scientific Computing, Vol. 1, No. 1, pp. 3–51. doi:10.1007/BF01061452 (1986)
 15. C. Teixeira, “*Incorporating Turbulence Models into the Lattice-Boltzmann Method*”, International Journal of Modern Physics C, Vol. 09, No. 08, pp. 1159–1175. doi:10.1142/S0129183198001060 (1998)
 16. D. Wilcox, “*Turbulence modelling for CFD (Third Edition)*”, DCW Industries, Incorporated (2006)
 17. B. Launder and D. Spalding, “*The numerical computation of turbulent flows*”, Computer Methods in Applied Mechanics and Engineering, Vol. 3, No. 2, pp. 269–289. doi:10.1016/0045-7825(74)90029-2 (1974)
 18. D. M. Freed, “*Lattice-Boltzmann method for macroscopic porous media modeling*”, International Journal of Modern Physics C, Vol. 9, No. 08, pp. 1491–1503 (1998)
 19. C. Sun, F. Pérot, R. Zhang, P. T. Lew, A. Mann, V. Gupta, D. M. Freed, I. Staroselsky and H. Chen, “*Lattice Boltzmann formulation for flows with acoustic porous media*”, Comptes Rendus Mécanique, Vol. 343, No. 10-11, pp. 533–544 (2015)
 20. G. Brès, F. Pérot and D. Freed, “*Properties of the Lattice–Boltzmann Method for Acoustics*”, 15th AIAA/CEAS Aeroacoustic Conference, Miami, Florida, pp. AIAA 2009–3395. doi:10.2514/6.2009-3395 (2009)
 21. J. Ffowcs Williams and D. Hawkings, “*Sound Generation by Turbulence and Surfaces in Arbitrary Motion*”, Philosophical Transactions of the Royal Society of London A: Mathematical, Physical and Engineering Sciences, Vol. 264, No. 1151 (2010)
 22. F. Farassat, and G. Succi, “*A review of propeller discrete frequency noise prediction technology with emphasis on two current methods for time domain calculations*,” Journal of Sound and Vibration, Vol. 71, No. 3, pp. 399–419 (1980)
 23. G. Brès, F. Pérot and D. Freed, “*A Ffowcs Williams-Hawkings solver for Lattice-Boltzmann based computational aeroacoustics*”, 16th AIAA/CEAS Aeroacoustic Conference, Stockholm, Sweden, pp. AIAA 2010–3711. doi:10.2514/6.2010-3711 (2010)

24. A. Najafi-Yazdi, G. Brès and L. Mongeau, “*An acoustic analogy formulation for moving sources in uniformly moving media*”, Proceedings of the Royal Society A: Mathematical, Physical and Engineering Sciences, Vol. 467, No. 2125, pp. 144–165. doi:10.1098/rspa.2010.0172 (2010)
25. D. Casalino, “*An advanced time approach for acoustic analogy predictions*”, Journal of Sound and Vibration, Vol. 261, No. 4, pp. 583–612. doi:10.1016/S0022-460X(02)00986-0 (2003)
26. T. Geyer, E. Sarradj and C. Fritzsche, “*Porous Airfoils: Noise Reduction and Boundary Layer Effects*”, International Journal of Aeroacoustics, Vol. 9, No. 6, pp. 787–820. doi:10.1260/1475-472x.9.6.787 (2010)
27. S. A. Showkat Ali, M. Azarpeyvand, C. M. Szőke and C. R. Ilário da Silva, “*Boundary layer flow interaction with a permeable wall*”, Physics of Fluids 30(8):085111. doi: 10.1063/1.5043276 (2018)
28. R. K. Amiet, “*Noise due to turbulent flow past a trailing edge*”, Journal of Sound and Vibration, Volume 47, No. 3, pp. 387-393 (1976)